COMMUNICATIONS PHYSICS

ARTICLE

https://doi.org/10.1038/s42005-019-0155-3 OPEN

# Fingerprints of an orbital-selective Mott phase in the block magnetic state of $BaFe_2Se_3$ ladders

N.D. Patel[1,2], A. Nocera[1,2], G. Alvarez[3], A. Moreo[1,2], S. Johnston[1,4] & E. Dagotto[1,2]

Resonant Inelastic X-Ray Scattering (RIXS) experiments on the iron-based ladder $BaFe_2Se_3$ unveiled an unexpected two-peak structure associated with local orbital (*dd*) excitations in a block-type antiferromagnetic phase. A mixed character between correlated band-like and localized excitations was also reported. Here, we use the density matrix renormalization group method to calculate the momentum-resolved charge- and orbital-dynamical response functions of a multi-orbital Hubbard chain. Remarkably, our results qualitatively resemble the $BaFe_2Se_3$ RIXS data, while also capturing the presence of long-range magnetic order as found in neutron scattering, only when the model is in an exotic orbital-selective Mott phase (OSMP). In the calculations, the experimentally observed zero-momentum transfer RIXS peaks correspond to excitations between itinerant and Mott insulating orbitals. We provide experimentally testable predictions for the momentum-resolved charge and orbital dynamical structures, which can provide further insight into the OSMP regime of $BaFe_2Se_3$.

[1] Department of Physics and Astronomy, The University of Tennessee, Knoxville, TN 37996, USA. [2] Materials Science and Technology Division, Oak Ridge National Laboratory, Oak Ridge, TN 37831, USA. [3] Computer Science & Mathematics Division and Center for Nanophase Materials Sciences, Oak Ridge National Laboratory, Oak Ridge, TN 37831, USA. [4] Joint Institute for Advanced Materials at The University of Tennessee, Knoxville, TN 37996, USA. Correspondence and requests for materials should be addressed to N.D.P. (email: npatel37@utk.edu)

The recent discovery of superconductivity in the two-leg iron-based ladder compounds $BaFe_2S_3$[1,2] and $BaFe_2Se_3$[3–5] opened an exciting new branch of research: these materials are the first members of the iron superconductors family[6–9] without iron layers, the parent compounds are insulators[1,2], and their low-dimensionality allows for accurate theoretical treatment[10–15]. For this reason, iron-ladder compounds were the focus of many recent experimental and theoretical studies[1–3,16–25]. In particular, inelastic neutron scattering data[23] is compatible with the exciting idea that $BaFe_2Se_3$ is in an orbital-selective Mott phase (OSMP) at ambient pressure[26–28], where one orbital is localized with a Mott gap while the others are gapless and itinerant (see Fig. 1). Moreover, this state displays an exotic magnetic order involving $2 \times 2$ ferromagnetic blocks that are antiferromagnetically staggered.

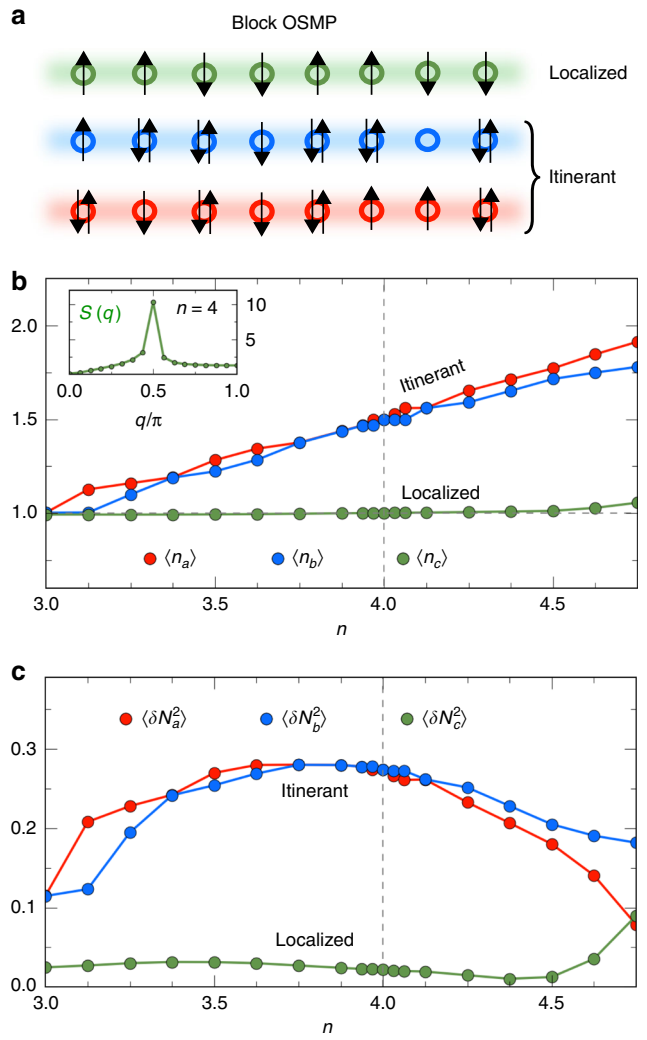


**Fig. 1** Local charge density and charge fluctuations. **a** Sketch of the block orbital selective Mott phase (OSMP) state of focus in the present effort. The upper orbital (green) is localized while the other two (blue, red) are itinerant. Illustration adapted from ref. [30]. **b** Average local occupation of each orbital vs overall electron density $n$, where $n = 4$ represents the filling of 4 electrons per site (using 32 sites), which is a realistic situation when a three-orbital model is used. The inset shows the total static spin-structure factor with a peak at $q = \pi/2$, representing the block-type antiferromagnetic order at $n = 4$, with two spins "up", followed by two "down", and then a repeated periodicity, as illustrated in (**a**) upper orbital. (**c**) Average local charge fluctuations on each orbital vs $n$

The intuitive origin of the block magnetic state admits multiple descriptions. Within Hartree-Fock treatments[21], the "block" structure arises from magnetic frustration because the system is located in parameter space between a ferromagnetic (FM) state, induced by double-exchange at large Hund coupling, and a staggered antiferromagnetic (AFM) state, induced by superexchange at small Hund coupling. Alternatively, recent efforts based on an itinerant perspective predicted that the metallic orbitals are the "drivers" while the localized spins are the "passengers", with the block structure arising from Fermi surface nesting[29]. From the experimental perspective, resonant inelastic x-ray scattering (RIXS) and X-ray photoemission (XPS) studies report the presence of both localized and itinerant carriers in $BaFe_2Se_3$, also suggesting OSMP physics;[24,25] however, up to now, no sufficient theoretical study has been carried out to support these indirect experimental claims of an OSMP ground state in $BaFe_2Se_3$. Our primary goal is to fill this gap and provide evidence from a theoretical perspective that indeed the "123" ladder is in an OSMP state.

One of the first steps towards unveiling the characteristic excitations of an OSMP state is to calculate its single-particle spectral function $A(\mathbf{q}, \omega)$ and its intra- and inter-orbital dynamical spin $S(\mathbf{q}, \omega)$, charge $N(\mathbf{q}, \omega)$, and orbital $L(\mathbf{q}, \omega)$ structure factors. Recently, theoretical predictions for $S(\mathbf{q}, \omega)$ were presented[30] in a block AFM OSMP. Using determinantal quantum Monte Carlo and the maximum entropy method, the low temperature $A(\mathbf{q}, \omega)$ was also reported employing an approximation to a multi-orbital Hubbard model[31]. However, $N(\mathbf{q}, \omega)$ and $L(\mathbf{q}, \omega)$, crucial for RIXS experiments, have not been addressed yet. Therefore, here for the first time, we use the density matrix renormalization group (DMRG) technique to compute the momentum-resolved charge and orbital response functions, as well as the single-particle spectral function (at zero temperature), of the block magnetic OSMP of a multi-orbital Hubbard chain.

There are multiple reasons for focusing on a chain geometry as opposed to a ladder. First, a three-orbital Hubbard chain is already equivalent to a three-leg one-orbital ladder; thus a three-orbital Hubbard ladder maps onto a six-leg one-orbital ladder, which is challenging even with DMRG. Second, in the usual "snake" geometry of DMRG, interorbital hoppings mutate into long-distance hoppings in the one-orbital chain analog, here involving sites effectively separated by eight lattice spacings. Such long-range hoppings compromise the accuracy of DMRG. Finally, RIXS in the eV scale usually addresses local excitations, and there should not be much difference between chains and ladders, as recent efforts in neutron scattering using both chains and ladders showed[30]. Our main goal is to understand the RIXS spectra in the case where no momentum is transferred along the leg direction of the $BaFe_2Se_3$[24] ladders ($q = 0$) allowing us to study a chain model as an approximation.

We compare our results against previously gathered RIXS data for $BaFe_2Se_3$[24], which measures magnetic, charge, and orbital excitations simultaneously[32–36]. By calculating the orbital response functions of the competing paramagnetic metal (PM) and FM insulator states, we show that block OSMP has a characteristic two-peak structure that is distinctive and in striking agreement with RIXS results on $BaFe_2Se_3$[24]. Moreover, we identify the observed *dd* peaks as orbital excitations between localized and itinerant orbitals. Our study strongly suggests that the ground state of $BaFe_2Se_3$ is indeed an OSMP with block magnetic order.

## Ground state results

Figure 1 plots the local charge occupation (panel b) and fluctuations (panel c) of each orbital vs the total electronic density,

which demonstrates that the OSMP is stable and robust against variations in the hole and electron doping[37]. First, we focus on the results for four electrons per site ($n = 4$), shown by the vertical dashed line in Fig. 1b, c (note that $n = 4$ in a three-orbital model is the analog of the realistic $n = 6$ in a five-orbital model). At this density, orbital $c$ has one electron per site, and thus becomes Mott localized, while the two other orbitals remain fractionally occupied, and thus metallic. The reason for this exotic behavior relies on the crystal-field splitting and different bandwidths of the orbitals: as the Hubbard $U$ interaction opens a gap and shifts energy states "up and down" relative to the gap, it becomes energetically favorable for orbital $c$ to have a half-filled lower Hubbard band, which is formed by moving electrons from the other bands into $c$. The corresponding intra-orbital charge fluctuations $\delta N_\gamma^2 = \langle n_\gamma^2 \rangle - \langle n_\gamma \rangle^2$ in orbital $c$ are significantly suppressed, compatible with a localized state, while charge fluctuations in orbitals $a$ and $b$ remain finite, compatible with a metallic state. The inset of Fig. 1b establishes the magnetic order at this filling, and plots the spin-structure factor at $n = 4$, displaying the characteristic peak at $q = \pi/2$ that is in agreement with the experimentally observed non-trivial block-type AFM order. Note that orbital $c$ (representing the $d_{xy}$ orbital, see methods) has the standard characteristics of a Mott phase at $n = 4$, where charge degrees of freedom are "frozen" (localized) and accompanied by well-formed local magnetic moments, $\mathbf{m}_c \sim 0.98\,\mu_B$. In contrast, the large local charge fluctuations of the other orbitals suggest a metallic behavior typical of itinerant electrons. The total on-site local moment at $n = 4$ is $\mathbf{m}_{\rm tot} \simeq 1.97\,\mu_B$, a robust value slightly larger than in experiments[17,18,23].

The coexistence of localized and itinerant carriers is also evident when examining the electronic density of each orbital vs the global filling near the commensurate value $n = 4$ (Fig. 1b). The linear behavior of $n_a$ and $n_b$ suggests a band-like picture, while the robust plateau in $n_c$ extending over a wide range of doping ($n = [3{:}4.5]$) indicates a Mott gap in the single-particle spectral function of orbital $c$. Since all these results provide ample evidence that we correctly capture the block-magnetic properties of $BaFe_2Se_3$, henceforth we fix the filling $n = 4$ to address the features of the block OSMP in the RIXS dynamical excitations, the focus of our publication.

## Dynamical spectra of the block OSMP

Figure 2a–k shows single-particle, charge, and orbital spectra along with schematic representations of corresponding excitations and real-space orbital fractionalization. We begin by describing the orbital-resolved single-particle spectral functions in Fig. 2d, e. Orbitals $a$ and $b$ have a finite quasi-particle weight at the Fermi level $E_F$, as also shown in the density-of-states in Fig. 3a, confirming once again the itinerant nature of electrons in these orbitals. Moreover, we find that the orbital $c$ has a gap of value $\Delta_c \sim 1.5$ eV (Note that the finite weight at μ in the c orbital is due to broadening) in $A^c(q, \omega)$ (Figs. 2e and 3a), compatible with our analysis in Fig. 1b, c. The spectral function demonstrates again the coexistence of gapped Mott (localized) and gapless

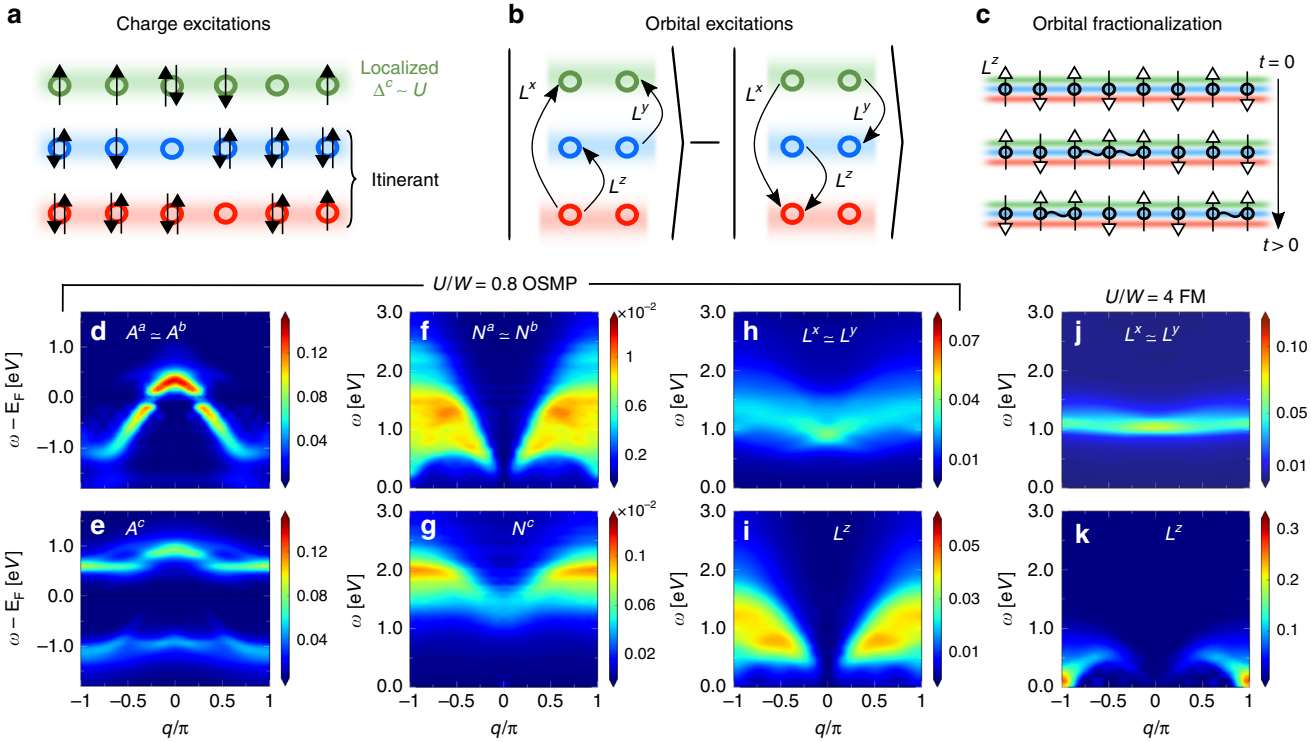


**Fig. 2** Single-particle spectra, charge excitations, and orbital excitations spectra. Sketches of **a** charge and **b** orbital excitations in a block orbital selective Mott phase (OSMP). **c** is a sketh of "orbital fractionalization" discussed in the ferromagnetic (FM) insulator context below. Actual density matrix renormalization group (DMRG) data shown correspond to the orbital-resolved, **d**, **e** single-particle spectra, **f**, **g** charge excitations, and **h**, **i** orbital excitations spectra within the block magnetic OSMP state. $A^{a/b}(q, \omega)$ has reduced but nonzero quasi-particle weight at the Fermi level ($E_F$) while $A^c(q, \omega)$ has a characteristic Mott gap $\Delta_c \sim 1.5$ eV. The charge excitations $N^{a/b}(q, \omega)$ have a gapless continuum at finite $\omega$ while $N^c(q, \omega)$ has an excitation gap of $\Delta_c^N \sim 1.5$ eV. $L^{x/y}(q, \omega)$ represents inter-orbital excitations between orbitals $a/b$ and $c$ ($d_{xz/yz} \leftrightarrow d_{xy}$) that are gapped with an excitation gap $\Delta^L \sim 0.7$–$0.9$ eV. $L^z(q, \omega)$ are inter-orbital excitations between orbitals $a$ and $b$ ($d_{xz} \leftrightarrow d_{yz}$). (**j**, **k**) Orbital excitations spectra within the FM insulator competing state. $L^{x/y}(q, \omega)$ has a gap ~0.9 eV and $L^z(q, \omega)$ is gapless with a robust $q = \pi$ peak indicating quasi-long range staggered orbital ordering. Spectral functions are calculated using $\Delta\omega = 0.05$ eV, broadening $\eta = 0.1$ eV, up to 1200 DMRG states, 24 sites (**d**–**g**), 16 sites (**h**–**k**), and 8 DMRG sweeps

itinerant carriers and agrees well with an earlier study of a similar model[31] (see Supplementary Note 1 for sum rule and finite size scaling analysis). Note also the presence of a pseudogap in the itinerant $d_{xz/yz}$ orbitals (not captured by earlier work[31]). It is likely that this pseudogap originates from correlations between the block ordered spins of Mott orbital $c$ and itinerant electrons in orbitals $a$ and $b$ (Fig. 3a), since they are not decoupled from one another. We also highlight that the Fermi momentum of orbitals $a$ and $b$ is approximately $q_F \simeq \pi/4$, leading to scattering at $2q_F \simeq \pi/2$ that is comparable to the spin-structure factor peak at $q = \pi/2$ corresponding to the block AFM order[29]. It is conceivable that the block phase of localized spins of the Mott orbital $c$ is driven by the Fermi nesting of itinerant orbitals, as in manganites and heavy-fermion systems[29]. In fact, recent experimental[23] and theoretical[30] work have confirmed that the magnetic excitations in $BaFe_2Se_3$ cannot be fully described using an effective Heisenberg model, highlighting the role of the other degrees of freedom in this material that we are focusing on here.

To arrive to our main conclusions, we now calculate the charge (Fig. 2f, g) and orbital (Fig. 2h, i) dynamics of the block-antiferromagnetic OSMP. Since the low-energy spin-dynamics have already been reported in the literature, we only focus on the high-energy charge and orbital dynamics that are more relevant to RIXS measurements at energy losses above 1 eV. As with $A^{a/b}(q, \omega)$, the charge excitations of the itinerant orbitals display a gapless continuum (Fig. 2f) because charge fluctuations can propagate freely in a metallic system (at fixed-energy transfer $\omega$ many states allow for charge fluctuations without an energy cost). In contrast to this, the charge excitations of the Mott orbital $c$ display a gap $\Delta_c^N \sim 1.5$ eV (Fig. 1g), and $N^c(q, \omega)$ shows incoherent charge excitations, compatible with doubly occupied orbitals $d_{xy}$ (i.e., $c$) configurations with an energy proportional to the Mott gap (Fig. 2a). We can contrast our results with the much studied one-orbital two-leg ladder Hubbard model, where charge excitations are gapped in the half-filled Mott phase but display a gapless continuum in the metallic phase away from half-filling[38]. Our results show the simultaneous presence of localized and itinerant fermions in our multi-orbital model.

Consider now the $q$-resolved orbital excitations in the block OSMP. Figure 2h ($L^{x/y}(q, \omega)$) shows the excitations from (to) the itinerant orbitals $a/b$ to (from) the localized orbital $c$. Figure 2i displays a gapless continuum in orbital excitations, $L^z(q, \omega)$, between the itinerant orbitals $a$ and $b$ (see illustration Fig. 2b). These dynamical spectra can be understood using the density-of-states (Fig. 3a), and poles of the single-particle spectral function of the OSMP (Fig. 3b). Figure 3a shows that electron scattering from $P_2 \rightarrow P_4$ requires an energy transfer ~0.9 eV (vertical arrow in Fig. 3b). This scattering creates a gapped response peak in the orbital excitations at $q \simeq 0$ and $\omega \simeq 0.9$ eV (Fig. 2h). The charge gap of orbital $c$ in $N^c(q, \omega)$ can also be understood via the scattering between points $P_1$ and $P_4$ of the density-of-states, shown by another vertical arrow in Fig. 3b. Additionally, the gapless continuum in $L^z(q, \omega)$ is very similar to the itinerant charge excitations, $N^{a/b}(q, \omega)$ because only the (almost degenerate) itinerant orbitals contribute in the calculations of $L^z(q, \omega)$.

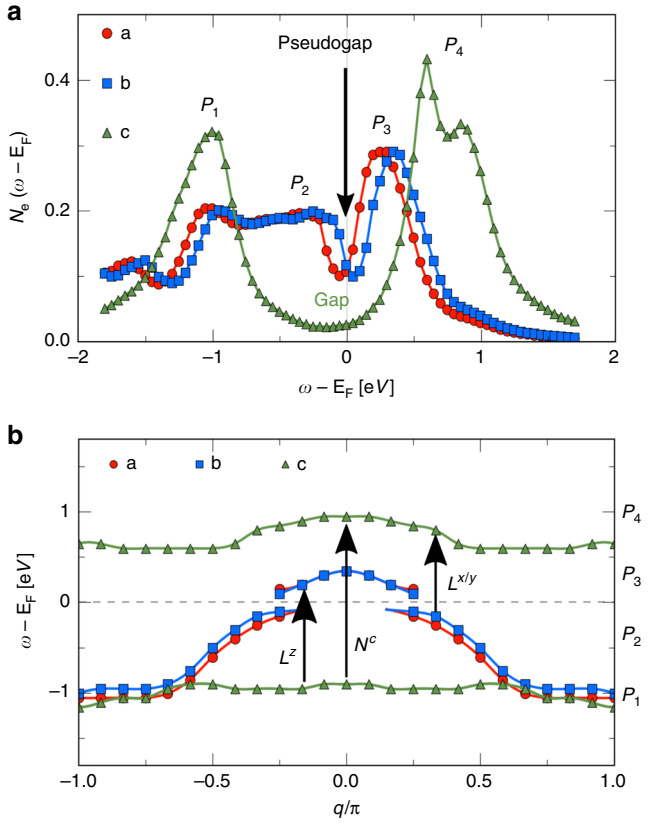


**Fig. 3** Single-particle states. Orbital-resolved **a** density of states, and **b** poles of the single-particle spectra of the block-antiferromagnetic orbital selective Mott phase. Various peaks in the density of states are labeled as $P_1$, $P_2$, $P_3$, and $P_4$. Arrows in the panel (**b**) represents various orbital and charge excitations as scattering between different bands. Calculations are performed using $\Delta\omega = 0.05$ eV, broadening $\eta = 0.1$ eV, 24 sites, and upto 1200 kept states with 8 sweeps

## Dynamical spectra of the FM insulator

To identify features of orbital excitations in the block OSMP that are unique, we also show the $q$-resolved orbital excitations in the competing FM insulator known to exist at $U/W = 4$[28], see Fig. 2j, k. In this FM phase, which is not yet known to be stable experimentally, theoretical calculations show that the single-particle spectral functions of all the orbitals have a Mott gap[31]. Figure 2j, k shows that the corresponding $L^{x/y}(q, \omega)$ and $L^z(q, \omega)$ display clearly sharper excitations in the FM phase in comparison to the block OSMP. Remarkably, $L^z(q, \omega)$ is gapless with a $\omega \simeq 0$ peak at $q = \pi$, implying quasi-long-range antiferro-orbital order in the ground state, as discussed before[31]. In fact, the $L^z(q, \omega)$ of this FM phase resembles the $S(q, \omega)$ of the spin-1/2 Heisenberg chain with a two-spinon continuum. By analogy, we conjecture that the $L^z(q, \omega)$ of the FM phase may denote the existence of fractionalized orbital excitations[39] (see illustration Fig. 2c). However, we expect that orbital fractionalization is intrinsic of a 1D problem, similar to spin fractionalization in 1D spin chains. Orbital and spin excitations were also studied recently in the context of Kugel-Khomskii models[40–42] where a single orbital flip fractionalizes into a spinon and an orbiton. This is different from our results where an orbital excitation is fractionalized into two orbitons. Here, we show novel results of orbital fractionalization in a FM insulator using a general multi-orbital fermionic Hamiltonian.

## Modelling RIXS

Our main result is in Fig. 4, where we compare the calculated orbital dynamical response vs RIXS Fe-$L_3$ edge experimental data for $BaFe_2Se_3$ at zero-momentum transfer[24]. Relating the full RIXS intensity to dynamical structure factors is not straightforward[35,43]. For example, for the single-band Hubbard model, the RIXS intensity can be directly related to dynamical structure factors only in limiting cases. To further complicate matters, the experimental effort[24] did not report the exact momentum transfer of the experiment. While the scattering

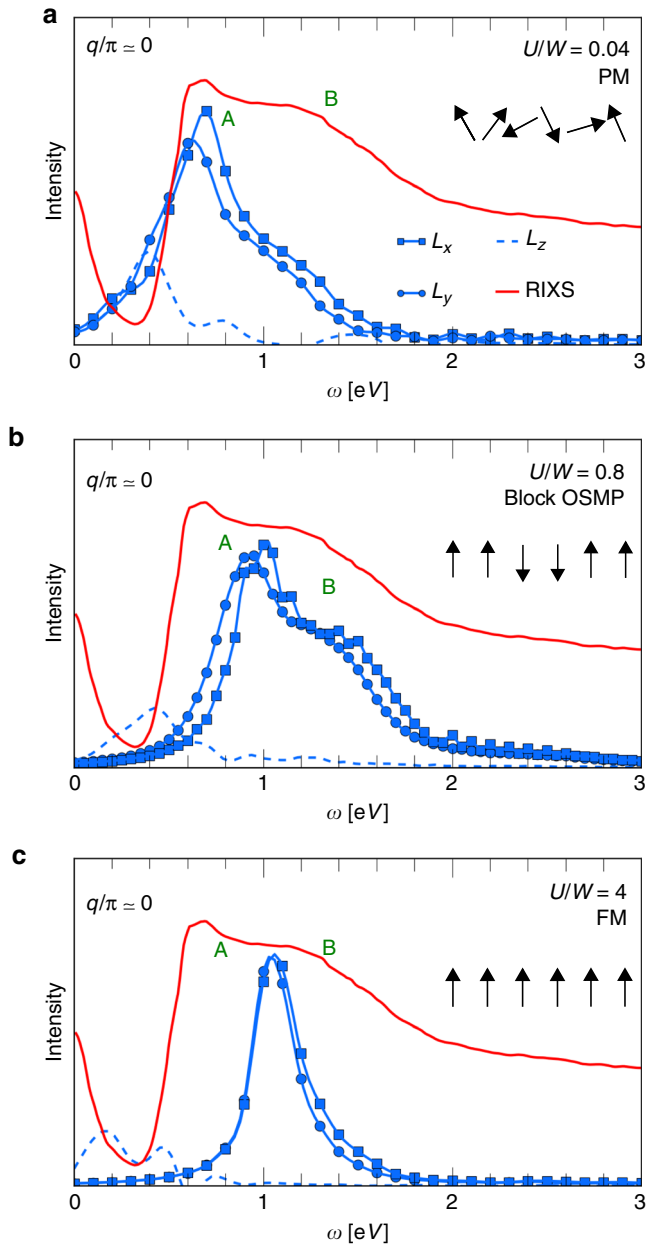


**Fig. 4** Comparison with resonant inelastic X-ray scattering (RIXS) experiments. Orbital excitations spectra (blue) at zero-momentum transfer corresponding to the three competing states, namely **a** $U/W = 0.04$ (paramagnetic phase), **b** $U/W = 0.8$ (block anti-ferromatic orbital selective Mott phase), and **c** $U/W = 4$ (ferromagnetic insulator), using DMRG and 16 sites. For comparison, each panel shows the experimental RIXS data (red) at the Fe-$L_3$ edge[24], where peaks *A* and *B* are *dd* excitations. Peak *A* and *B* are believed to be caused by electron scattering from (to) intinerant orbitals to (from) Mott orbital ($P_2 \rightarrow P_4$ and $P_1 \rightarrow P_3$ excitations shown in the density of states calculations)

geometry employed nominally probes $q = 0$ excitations along the chain, there were difficulties in aligning the chain orientation during beam time and some finite $q$ excitations may have been mixed into the spectra. Additionally, RIXS measures excitations of many different channels (e.g., spin, charge, and orbital), making it difficult to differentiate between those distinct channels. However, comparisons with the dynamical response functions can still provide at least qualitative insights into the dominant features and energy scales of RIXS experiments. Moreover, a merit of our effort is that we calculate excitations for each channel separately, and can, therefore, provide detailed predictions for future experiments. Until additional data become available our focus on RIXS experiments at $q = 0$ momentum transfer[24] is the natural avenue to pursue.

At zero energy transfer, there is an "elastic" peak commonly observed in RIXS experiments. We note that magnon contributions to the RIXS data generally occur at energy losses $\omega < 0.2$ in the Fe-based superconductors, and, therefore, are hidden in the elastic contribution in the RIXS experiment[23,24,30]. For this reason, this low-energy region will not be our focus. To identify the unique features of orbital excitations in the block OSMP ($U/W = 0.8$), we also present results for the PM ($U/W = 0.04$) and FM ($U/W = 4$) competing phases (Fig. 4a–c). Overall, we find a close agreement between our dynamical spectra in the block OSMP at $q \simeq 0$ and the two-peak structure observed in experiments, involving localized *dd* excitations of the iron 3*d* orbitals. The OSMP two-peak structure (Fig. 4b) is distinct from that in the FM phase, where the two peaks are almost identical in position and width. With regards to the PM phase results (Fig. 4a), there are some similarities with the spectra shape of the OSMP phase. The presence of these similarities are natural since according to ref. [28] at $U/W = 0.04$ the population of orbital $c$ is already near 1, although the block magnetic phase is still not fully developed. One might argue that the PM regime data could also fit the experiments with appropriate broadening, particularly considering that high-frequency results involving interorbital excitations do not typically change abruptly across phase transitions; however, neutron scattering experiments tell us that the material is magnetically ordered in a block state. Thus the PM state cannot be chosen as the correct state even though the RIXS data might be consistent with our predicted dynamical spectra.

Our model suggests that the experimentally observed peaks represent excitations between localized $d_{xy}$ and itinerant $d_{xz/yz}$ orbitals. They are gapped with an activation energy 0.7–0.9 eV in the calculations, and ~0.35–0.45 eV in the experiments (transitions involving $e_g$ orbitals, outside our model, should appear at higher energies). The difference in absolute gap numbers could be fixed by tuning our model parameters still within the OSMP phase (or by using ladders instead of chains, which is technically much harder, as discussed before). Since "fine tuning" is not our goal, but a qualitative understanding of results, we consider our (already costly) simulation results sufficient for our main qualitative conclusion: the block OSMP is the one that most closely resembles the experimental data. In addition, in the real samples, there is broadening due to phonons and non-crystallinity effects that could make it challenging to define the magnitude of the gap accurately. Regardless, it is clear from experiments that there is a gap in the RIXS $q = 0$ response. However, the paramagnetic phase has a gapless $q = 0$ response in $L^{x/y}(q \simeq 0, \omega)$ (Fig. 4a), even-though there is a precursor to a two-peak structure, establishing another difference with the OSMP results. Moreover, while the FM insulator shows a gapped $L^{x/y}(q \simeq 0, \omega)$ response, this is with the presence of a single peak at $\omega \simeq 1$ eV. In summary, the gapped two-peak response is only evident in the block OSMP phase.

## Discussion

Our results suggest that the experimentally observed gap is not a conventional semi-conducting gap, but instead originates from the inter-orbital excitations of a magnetically ordered OSMP. Figure 4b shows that peak *A* occurs at ~0.9 eV, for the zero momentum transfer, as a result of vertical ($\Delta q = 0$) scattering across $E_F$ from the itinerant $d_{xz/yz}$ orbitals to the $d_{xy}$ Mott orbital (Fig. 3b, $P_2 \rightarrow P_4$). The shoulder/peak labeled as *B* represents scattering from the localized $d_{xy}$ band below $E_F$ to the itinerant

hole pocket bands $d_{xz/yz}$ above $E_F$, with zero momentum transfer $q/\pi = 0$ (Fig. 3b, $P_1 \rightarrow P_3$). These peaks cannot be described using a simple weak-coupling framework.

The orbital $d_{xy}$ charge excitations in our calculations generate a response at $\omega = 1.4$ eV of intensity ~100 times smaller than the orbital excitations (Fig. 2f, i). This is because local charge fluctuations are suppressed significantly in the Mott orbital, namely the probabilities associated with a doubly occupied or empty site configuration are small compared to configurations where sites are half-filled. Additionally, the features in $N^{a/b}(q, \omega)$ and $L^z(q, \omega)$ originate from itinerant carriers that are sensitive to the incident x-ray energy ($\hbar\omega_{in}$) of the RIXS experiments. It is known that localized excitations do not shift with $\hbar\omega_{in}$, while itinerant carriers produce a response that shifts linearly with $\hbar\omega_{in}$, becoming part of the fluorescence at large $\hbar\omega_{in}$[44]. Therefore, the $L^z(\mathbf{q}, \omega)$ peak at the low-energy transfer $\omega$ (Fig. 4b, dashed) will shift with the incident energy. The same is true for itinerant charge excitations $N^{a/b}(q, \omega)$. In fact, RIXS experiment on $BaFe_2Se_3$ also find (fluorescence) peaks that shift with incident energy and merge with the localized excitations (A and B of Fig. 4b), suggesting the existence of both localized and itinerant degrees of freedom at the experimental low temperature, as also found for the OSMP regime in our calculations.

To understand better the characteristics of the states at peak positions $A$ and $B$, we also show real-space $L_{x/y}$ orbital correlations vs energy transfer at fixed distances (first to fourth nearest neighbor) in Fig. 5. In the block OSMP the high-energy states at peak $A$ have positive $L_{x/y}$ correlations up to the fourth nearest neighbor in real-space, while states at peak $B$ have negative $L_{x/y}$ correlations only up to the nearest neighbor. In Fig. 5, we explicitly show that the peak $A$ of the block OSMP represents states with ferro-orbital ordering, while $B$ represents states with short-range anti-ferro-orbital fluctuations. However, the ground state of block OSMP does not have an orbital ordering unlike the ground-state of the competing FM insulator at $U/W = 4$, which has uniform magnetic[28] and staggered $L_z$ orbital order (Fig. 2h). For the $U/W = 4$ FM case, the corresponding $L_{x/y}$ is gapped and has excitations only at $\omega \sim 1.0$ (Fig. 2h). In real-space, these high-energy states show short-range positive correlations, persisting only up to the second nearest neighbor (not shown).

In conclusion, we calculated the momentum-resolved orbital and charge dynamics of an OSMP using the three $t_{2g}$ orbitals, and compared our results to the available RIXS data for $BaFe_2Se_3$ at zero momentum transfer[24]. We find localized $dd$ excitations that produce particular peaks $A$ and $B$ that are very similar to those observed experimentally, providing theoretical support that $BaFe_2Se_3$ is indeed an orbital-selective Mott insulator. Moreover, we predict the $q$-resolved charge and orbital dynamical spectra that can be measured by RIXS in the future. Recent RIXS experiments display a very similar response for $BaFe_2Se_3$ and $BaFe_2S_3$, implying that an orbital-selective phase is present in the $BaFe_2S_3$ high-pressure superconductor as well[1,45]. We encourage the measurement of the band structure and density-of-states of these materials using angle-resolved photoemission and scanning tunneling microscopy, to confirm our predicted band(s) crossing of the Fermi surface and Mott like band(s) below the Fermi surface. We also encourage future $q$-resolved RIXS measurements for $BaFe_2Se_3$ and $BaFe_2S_3$ compounds. Finally, the novel orbital fractionalization proposed in the FM insulator phase defines a new avenue of research that will be pursued soon.

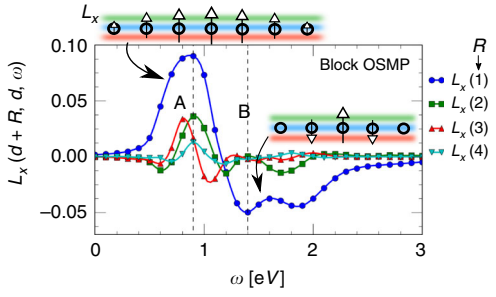


**Fig. 5** Real-space orbital correlations. Real-space $L_x(d + R, d, \omega)$ [using $O_i = L^x_{d+R}$ and $O_j = L^x_d$ in Eq. (1)] vs. $\omega$ with a fixed center site $d = 8$ on a 16-sites three-orbital chain in the block antiferromagnetic orbital selective Mott phase ($U/W = 0.8$). Labels $A$ and $B$ (vertical dashed line) show the peak positions labels. Overall negative (positive) response denote local antiferro (ferro) orbital ordering. The cartoons represent pictorially the $L_{x/y}$ correlations described in the text that characterize the A and B states

## Methods

**Model**. We use a multi-orbital Hubbard model composed of kinetic energy and interaction terms as $H = H_K + H_I$. The kinetic energy part of the Hamiltonian is

$$H_K = \sum_{i,\sigma,\gamma,\gamma'} t^{\gamma\gamma'}(c^\dagger_{i\gamma\sigma}c_{i+1\gamma'\sigma} + \text{H.c.}) + \sum_{i,\sigma,\gamma}\epsilon_\gamma n_{i\sigma\gamma},$$

where $c^\dagger_{i\gamma\sigma}$ ($c_{i\gamma\sigma}$) creates (destroys) an electron at site $i$, orbital $\gamma$, and spin $\sigma$. The first term represents nearest-neighbor electron hopping from orbital $\gamma'$ to $\gamma$ with a hopping amplitude $t^{\gamma\gamma'}$. We denote the relevant orbitals $d_{xz}$, $d_{yz}$, and $d_{xy}$ as $a$, $b$, and $c$, respectively. The second term contains the orbital-dependent crystal-field splitting. The parameters are (eV units) $\varepsilon_a = -0.1$, $\varepsilon_b = 0.0$, $\varepsilon_c = 0.8$, $t^{aa} = t^{bb} = 0.5$, $t^{cc} = 0.15$, and $t^{ac} = t^{bc} = t^{ca} = t^{cb} = -0.10$. The non-interacting bandwidth is $W = 4.9t^{aa}$. This set of parameters is known[28] to produce bands that emulate iron-based superconductors, with hole pockets at $q = 0$ and an electron pocket at $q = \pm\pi$[8]. Our reported results are all at zero temperature.

The interaction term, in standard notation, is

$$H_I = U\sum_{i,\gamma} n_{i\gamma\uparrow}n_{i\gamma\downarrow} + \left(U' - \frac{J_H}{2}\right)\sum_{i,\gamma<\gamma'} n_{i\gamma}n_{i\gamma'} - 2J_H\sum_{i,\gamma<\gamma'}\mathbf{S}_{i\gamma}\cdot\mathbf{S}_{i\gamma'} + J_H\sum_{i,\gamma<\gamma'}(P^\dagger_{i\gamma}P_{i\gamma'} + \text{H.c.}).$$

The first term is the intraorbital Hubbard repulsion $U$. The second is the interorbital repulsion between electrons at different orbitals, with $U' = U - 2J_H$. The third term is the Hund's coupling $J_H$, and the last term represents the on-site interorbital hopping of electron pairs ($P_{i\gamma'} = c_{i\gamma'\uparrow}c_{i\gamma'\downarrow}$). Explicit definitions for all the operators in the model are in the Supplementary Notes 2. The rich physical properties realized by this model were discussed extensively in ref. [28]. Most of the data presented here was gathered at $J_H/U = 0.25$ (as used extensively before refs. [28,46,47]) and $U/W = 0.8$ where the block-type AFM OSMP is known to be stable[28]. However, we also show results for the paramagnetic metal (PM, small $U$) and ferromagnetic insulator (FM, large $U$) phases to highlight unique features of the block OSMP by contrast.

**Observables**. To characterize the OSMP, we calculate the dynamical response functions

$$O(i,j,\omega) = \frac{-1}{\pi}\text{Im}\left[\left\langle\psi_0\middle|O_i^\dagger\frac{1}{\omega - H + E_g + i\eta}O_j\middle|\psi_0\right\rangle\right] \quad (1)$$

using DMRG within the correction-vector formulation in Krylov space[48,49]. The single-particle photoemission spectral function is obtained using $O_i = c_{i\sigma\gamma}$. The intraorbital particle-hole (charge) excitations arise using $O_i = \sum_\sigma n_{i\sigma\gamma} - n_{i\sigma\gamma}$, where we explicitly subtract the ground-state contribution to measure only the fluctuations. Finally, the orbital excitations are obtained using $O_i = \{L^x_i, L^y_i, L^z_i\}$, where

$$\begin{aligned} L^x_i &= i\sum_\sigma(c^\dagger_{ia\sigma}c_{ic\sigma} - c^\dagger_{ic\sigma}c_{ia\sigma}),\\ L^y_i &= i\sum_\sigma(c^\dagger_{ib\sigma}c_{ic\sigma} - c^\dagger_{ic\sigma}c_{ib\sigma}),\\ L^z_i &= i\sum_\sigma(c^\dagger_{ia\sigma}c_{ib\sigma} - c^\dagger_{ib\sigma}c_{ia\sigma}). \end{aligned} \quad (2)$$

These operators are derived from the $L = 2$ angular momentum operators in the $t_{2g}$ orbital basis, see Supplementary Note 3.

## Data availability

The sample inputs and corresponding computational details for reproducing the presented data can be found at https://g1257.github.io/papers/86/.

## Code availability

Computer codes used in this study are available at https://g1257.github.io/dmrgPlusPlus/.

Received: 16 November 2018 Accepted: 29 April 2019
Published online: 21 June 2019

## References


1. Takahashi, H. et al. Pressure-induced superconductivity in the iron-based ladder material $BaFe_2S_3$. *Nat. Mater.* **14**, 1008 (2015).
2. Yamauchi, T., Hirata, Y., Ueda, Y. & Ohgushi, K. Pressure-induced Mott transition followed by a 24-K superconducting phase in $BaFe_2S_3$. *Phys. Rev. Lett.* **115**, 246402 (2015).
3. Ying, J., Lei, H., Petrovic, C., Xiao, Y. & Struzhkin, V. V. Interplay of magnetism and superconductivity in the compressed Fe-ladder compound $BaFe_2Se_3$. *Phys. Rev. B* **95**, 241109 (2017).
4. Zhang, Y., Lin, L.-F., Zhang, J.-J., Dagotto, E. & Dong, S. Sequential structural and antiferromagnetic transitions in $BaFe_2Se_3$ under pressure. *Phys. Rev. B* **97**, 045119 (2018).
5. Svitlyk, V. et al. Crystal structure of $BaFe_2Se_3$ as a function of temperature and pressure: phase transition phenomena and high-order expansion of Landau potential. *J. Phys.: Condens. Matter* **25**, 315403 (2013).
6. Basov, D. & Chubukov, A. V. Manifesto for a higher $T_c$. *Nat. Phys.* **7**, 272 (2011).
7. Fernandes, R. M. & Chubukov, A. V. Low-energy microscopic models for iron-based superconductors: a review. *Rep. Prog. Phys.* **80**, 014503 (2017).
8. Dai, P., Hu, J. & Dagotto, E. Magnetism and its microscopic origin in iron-based high-temperature superconductors. *Nat. Phys.* **85**, 709–718 (2012).
9. Dagotto, E. Colloquium: the unexpected properties of alkali metal iron selenide superconductors. *Rev. Mod. Phys.* **85**, 849–867 (2013).
10. White, S. R. Density matrix formulation for quantum renormalization groups. *Phys. Rev. Lett.* **69**, 2863–2866 (1992).
11. Schollwöck, U. The density-matrix renormalization group. *Rev. Mod. Phys.* **77**, 259–315 (2005).
12. White, S. R. Density matrix renormalization group algorithms with a single center site. *Phys. Rev. B* **72**, 180403 (2005).
13. White, S. R. Spin gaps in a frustrated Heisenberg model for $CaV_4O_9$. *Phys. Rev. Lett.* **77**, 3633–3636 (1996).
14. Alvarez, G. The density matrix renormalization group for strongly correlated electron systems: A generic implementation. *Comput. Phys. Commun.* **180**, 1572–1578 (2009).
15. D'Azevedo, E. F., Elwasif, W. R., Patel, N. D. & Alvarez, G. Targeting multiple states in the density matrix renormalization group with the singular value decomposition. Preprint at https://arxiv.org/abs/1902.09621 (2019).
16. Patel, N. D. et al. Magnetic properties and pairing tendencies of the iron-based superconducting ladder $BaFe_2S_3$: combined ab initio and density matrix renormalization group study. *Phys. Rev. B* **94**, 075119 (2016).
17. Nambu, Y. et al. Block magnetism coupled with local distortion in the iron-based spin-ladder compound $BaFe_2Se_3$. *Phys. Rev. B* **85**, 064413 (2012).
18. Caron, J. M., Neilson, J. R., Miller, D. C., Llobet, A. & McQueen, T. M. Iron displacements and magnetoelastic coupling in the antiferromagnetic spin-ladder compound $BaFe_2Se_3$. *Phys. Rev. B* **84**, 180409 (2011).
19. Lei, H., Ryu, H., Frenkel, A. I. & Petrovic, C. Anisotropy in $BaFe_2Se_3$ single crystals with double chains of FeSe tetrahedra. *Phys. Rev. B* **84**, 214511 (2011).
20. Caron, J. M. et al. Orbital-selective magnetism in the spin-ladder iron selenides $Ba_{1-x}K_xFe_2Se_3$. *Phys. Rev. B* **85**, 180405 (2012).
21. Luo, Q. et al. Magnetic states of the two-leg-ladder alkali metal iron selenides $AFe_2Se_3$. *Phys. Rev. B* **87**, 024404 (2013).
22. Patel, N. D., Nocera, A., Alvarez, G., Moreo, A. & Dagotto, E. Pairing tendencies in a two-orbital Hubbard model in one dimension. *Phys. Rev. B* **96**, 024520 (2017).
23. Mourigal, M. et al. Block magnetic excitations in the orbitally selective Mott insulator $BaFe_2Se_3$. *Phys. Rev. Lett.* **115**, 047401 (2015).
24. Monney, C. et al. Resonant inelastic X-ray scattering at the Fe $L_3$ edge of the one-dimensional chalcogenide $BaFe_2Se_3$. *Phys. Rev. B* **88**, 165103 (2013).
25. Ootsuki, D. et al. Coexistence of localized and itinerant electrons in $BaFe_2X_3$ ($X$ = S and Se) revealed by photoemission spectroscopy. *Phys. Rev. B* **91**, 014505 (2015).
26. Georges, A., dé Medici, L. & Mravlje, J. Strong correlations from Hund's coupling. *Annu. Rev. Condens. Matter Phys.* **4**, 137–178 (2013). And references therein.
27. Yu, R. & Si, Q. Orbital-selective Mott phase in multiorbital models for alkaline iron selenides $K_{1-x}Fe_{2-y}Se_2$. *Phys. Rev. Lett.* **110**, 146402 (2013).
28. Rincón, J., Moreo, A., Alvarez, G. & Dagotto, E. Exotic magnetic order in the orbital-selective Mott regime of multiorbital systems. *Phys. Rev. Lett.* **112**, 106405 (2014).
29. Herbrych, J. et al. Novel magnetic block states in low-dimensional iron-based superconductors. Preprint at https://arxiv.org/abs/1812.00325 (2018).
30. Herbrych, J. et al. Spin dynamics of the block orbital-selective Mott phase. *Nat. Commun.* **9**, 3736 (2018).
31. Li, S. et al. Nonlocal correlations in the orbital selective Mott phase of a one-dimensional multiorbital Hubbard model. *Phys. Rev. B* **94**, 235126 (2016).
32. Ament, L. J. P., van Veenendaal, M., Devereaux, T. P., Hill, J. P. & van den Brink, J. Resonant inelastic X-ray scattering studies of elementary excitations. *Rev. Mod. Phys.* **83**, 705–767 (2011).
33. Wohlfeld, K., Nishimoto, S., Haverkort, M. W. & van den Brink, J. Microscopic origin of spin-orbital separation in $Sr_2CuO_3$. *Phys. Rev. B* **88**, 195138 (2013).
34. Marra, P., Wohlfeld, K. & van den Brink, J. Unraveling orbital correlations with magnetic resonant inelastic X-ray scattering. *Phys. Rev. Lett.* **109**, 117401 (2012).
35. Jia, C. et al. Persistent spin excitations in doped antiferromagnets revealed by resonant inelastic light scattering. *Nat. Commun.* **5**, 3314 (2014).
36. Johnston, S. et al. Electron-lattice interactions strongly renormalize the charge-transfer energy in the spin-chain cuprate $Li_2CuO_2$. *Nat. Commun.* **7**, 10563 (2016).
37. For an analysis of the full phase diagram varying the electronic density, and for a discussion of several OSMP states see Rincón, J. et al. Quantum phase transition between orbital-selective Mott states in Hund's metals *Phys. Rev. B* **90**, 241105 (2014).
38. Nocera, A. et al. Doping evolution of charge and spin excitations in two-leg Hubbard ladders: Comparing DMRG and FLEX results. *Phys. Rev. B* **97**, 195156 (2018).
39. Schlappa, J. et al. Spin-orbital separation in the quasi-one-dimensional Mott insulator $Sr_2CuO_3$. *Nature* **485**, 82 (2012).
40. Chen, C.-C., van Veenendaal, M., Devereaux, T. P. & Wohlfeld, K. Fractionalization, entanglement, and separation: understanding the collective excitations in a spin-orbital chain. *Phys. Rev. B* **91**, 165102 (2015).
41. Wohlfeld, K., Daghofer, M., Nishimoto, S., Khaliullin, G. & van den Brink, J. Intrinsic coupling of orbital excitations to spin fluctuations in mott insulators. *Phys. Rev. Lett.* **107**, 147201 (2011).
42. Heverhagen, J. & Daghofer, M. Spinon-orbiton repulsion and attraction mediated by Hund's rule. *Phys. Rev. B* **98**, 085120 (2018).
43. Jia, C., Wohlfeld, K., Wang, Y., Moritz, B. & Devereaux, T. P. Using RIXS to uncover elementary charge and spin excitations. *Phys. Rev. X* **6**, 021020 (2016).
44. Bisogni, V. et al. Ground-state oxygen holes and the metal-insulator transition in the negative charge-transfer rare-earth nickelates. *Nat. Commun.* **7**, 13017 (2016).
45. Takubo, K. et al. Orbital order and fluctuations in the two-leg ladder materials $BaFe_2X_3$ ($X$ = S and Se) and $CsFe_2Se_3$. *Phys. Rev. B* **96**, 115157 (2017).
46. Haule, K. & Kotliar, G. Coherence-incoherence crossover in the normal state of iron oxypnictides and importance of Hund's rule coupling. *New J. Phys.* **11**, 025021 (2009).
47. Luo, Q. et al. Neutron and ARPES constraints on the couplings of the multiorbital Hubbard model for the iron pnictides. *Phys. Rev. B* **82**, 104508 (2010).
48. Nocera, A. & Alvarez, G. Spectral functions with the density matrix renormalization group: Krylov-space approach for correction vectors. *Phys. Rev. E* **94**, 053308 (2016).
49. Kühner, T. D. & White, S. R. Dynamical correlation functions using the density matrix renormalization group. *Phys. Rev. B* **60**, 335–343 (1999).


## Acknowledgements

We thank C. Monney and T. Schmitt for providing a copy of the experimental data shown in Fig. 4. N.D.P., A.N., A.M., and E.D. were supported by the U.S. Department of Energy (DOE), Office of Science, Basic Energy Sciences (BES), Materials Science and Engineering Division. G.A. and S.J. were supported by the Scientific Discovery through Advanced Computing (SciDAC) program funded by the U.S. Department of Energy, Office of Science, Advanced Scientific Computing Research and Basic Energy Sciences, Division of Materials Sciences and Engineering. N.D.P. was also partially supported by the National Science Foundation Grant No. DMR-1404375. Part of this work was conducted at the Center for Nanophase Materials Sciences, sponsored by the Scientific User Facilities Division (SUFD), BES, DOE, under contract with UT-Battelle. Computer time provided in part by resources supported by the University of Tennessee and Oak Ridge National Laboratory Joint Institute for Computational Sciences.

## Author contributions

N.D.P. and E.D. planned the project. N.D.P. performed all the DMRG calculations for multi-orbital Hubbard model. A.N. and G.A. developed the DMRG++ computer

program. E.D., A.M., and S.J. provided important insight into the understanding of orbital excitations, and comparison with RIXS experiment.

## Additional information

**Supplementary information** accompanies this paper at https://doi.org/10.1038/s42005-019-0155-3.

**Competing interests:** The authors declare no competing interests.

**Reprints and permission** information is available online at http://npg.nature.com/reprintsandpermissions/

**Publisher's note:** Springer Nature remains neutral with regard to jurisdictional claims in published maps and institutional affiliations.